Chapter 2
Fluid Transport Mechanisms in Paper-Based Microfluidic Devices

Sanjay Kumar, Pulak Bhushan and Shantanu Bhattacharya

Abstract Paper microfluidics is one of the rapidly growing technology and shown a tremendous caliber in field of healthcare, biochemistry, environmental monitoring, analytical chemistry, etc. Owing to their distinct advantages such as rapid, easy-to-use, compatible with biological, organic and inorganic entities, chemical inertness, robustness, economical, environment-friendly and easy disposal, paper microfluidic-based devices have become a prominent alternative for existing technologies POC technologies. The challenge remains, however, in the designing of an efficient paper-based device for specific applications. A great deal of work has been done in this field to address the challenges in its two key enabling parameters namely 'materials properties' and 'fluid-transport mechanism' to achieve the functional paper device in an efficient and predictive way. Keeping in mind the previously published articles, the focus here is primarily on showcasing the fluid transport mechanisms through paper-based microfluidic devices. This chapter intends to provide an understanding towards theoretical modelling from a device perspective. The commonly used paper substrates and critical factors involved with any fluid transport phenomena is also covered.

Keywords Paper microfluidic · Fluid transport · Capillary flow · Lucas-Washburn equation · Paper types

S. Kumar and P. Bhushan have equal contribution in this chapter.

S. Kumar (✉) · P. Bhushan · S. Bhattacharya
Microsystems Fabrication Laboratory, Department of Mechanical Engineering, Indian Institute of Technology, Kanpur, Uttar Pradesh 208016, India
e-mail: sanjay21505@gmail.com

S. Kumar
Department of Mechanical Engineering, National University of Singapore, 9 Engineering Drive 1, Singapore 117575, Singapore

P. Bhushan
Department of Electrical & Computer Engineering, Florida International University, Miami, FL 33199, USA

S. Bhattacharya et al. (eds.), *Paper Microfluidics*, Advanced Functional Materials and Sensors, https://doi.org/10.1007/978-981-15-0489-1_2

2.1 Introduction

Paper is a thin, lightweight ($\sim$10 mg cm^{-2}) and flexible material, available in a wide range of thicknesses (Martinez et al. 2009). It is produced by pressing together multiple cellulose fibers with a porous structure (Altundemir et al. 2017). Although a variety of paper substrates is available in the market, among them, mainly two types of paper substrates are used in point-of-care diagnostics—pure cellulose fiber-based materials (filter paper, chromatography paper, etc.) and nitric acid treated cellulose-based materials (nitrocellulose membrane). Cellulose fiber is a linear chain macromolecule composed of β-D-glucopyranose units linked by glycosidic bonds (O'sullivan 1997). It is made from various raw sources such as wood, flax, cotton, jute, bamboo, grass, bagasse (Yetisen et al. 2013), etc. Cellulose is inherently fibrous, hydrophilic, tough, biodegradable and water-insoluble substance. In filter papers, fibers are randomly overlapped over each other (Fig. 2.1a–c) while in nitrocellulose membrane, fibers are granular in shape (Fig. 2.1d). Filter papers such as Whatman filter paper (grade 1–4) are generally used in qualitative analytical techniques for analyte detection. Owing to its wicking ability, filter paper is the most widely used substrate in the fabrication of paper-based devices (Martinez et al. 2009; Liana et al. 2012).

Nitrocellulose, is a microporous structure which is manufactured by partial nitration of refined cellulose (nitration ratio <2.3 substitutions per ring) (Mansfield 2005). Nitration alters the properties of cellulose such as from hydrophilic to hydrophobic and makes it highly adsorbable to proteins. Nitrocellulose membrane is widely used in lateral flow assay based biosensors (Fenton et al. 2008). Nitrocellulose membrane is brittle and weak. The lower tensile strength of nitrocellulose membranes (<2 lb/in) make them very difficult to handle. Therefore, adhesive polyester film backing is generally used to strengthen the nitrocellulose membrane (Mansfield 2009). Table 2.1 shows a summary of different types of paper substrate, their characteristics, and broad applications.

The selection of paper substrate in biosensing depends on various characteristics such as capillary flow time (the time required for a liquid sample to flow through the pores in the lateral direction), thickness of the paper, pore size, porosity (% of air present in porous structure) and surface quality. The capillary flow time is inversely related to the capillary flow rate and expressed as s cm^{-1}. Practically the capillary flow rate is difficult to measure accurately because the fluid flow rate through the nitrocellulose membrane decays exponentially as the fluid front transports along it. The estimation of capillary flow time helps in deciding the position of test line and control line on the membrane.

Paper thickness is another critical parameter for paper-based microfluidic devices for several reasons. The amount of sample required for a successful run of the assay depends on the pore volume. A thick membrane would need higher sample volume for the saturation of pores. But if the membrane thickness is too thin, then the membrane will be weak and might get damaged during handling. Also, when the known volume of capture reagent (Ab/Ag, in case of LFA) is either printed or

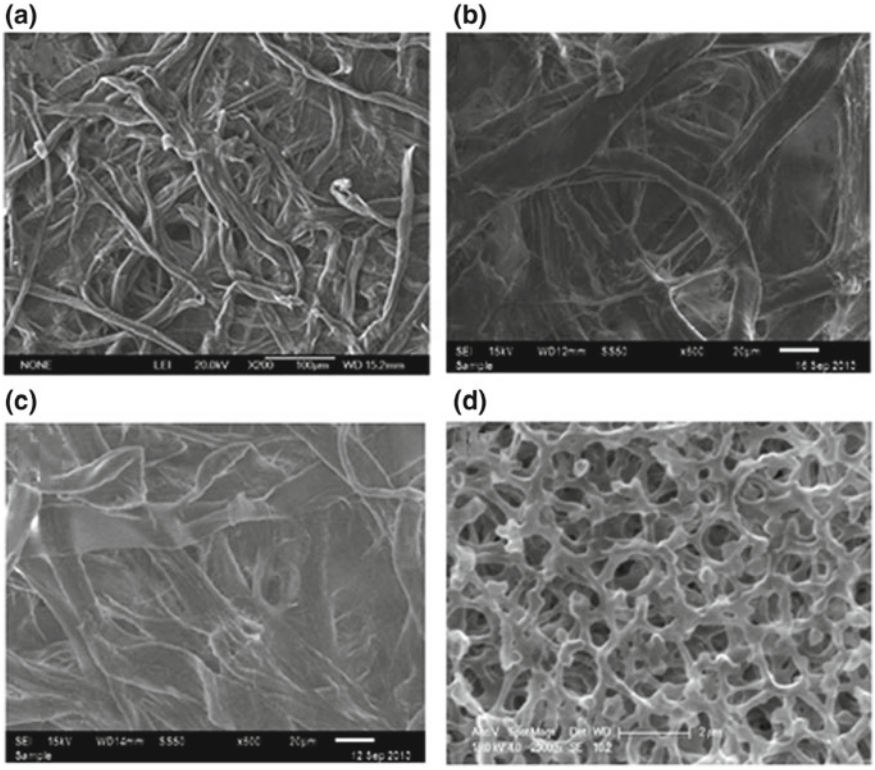

Fig. 2.1 SEM images of Whatman filter paper **a** Grade 1 at 200× magnification. Reprinted with the permission from Liu et al. (2015) ©Elsevier Ltd., 2014. **b** Grade 3 at 600× magnification (fiber thickness: 14.8 ± 1.4 μm) and **c** Grade 4 at 600× magnification (fiber thickness of 20.4 ± 3.6 μm). Adapted with permission from Evans et al. (2014) ©The Royal Society of Chemistry, 2014. **d** SEM images of nitrocellulose membrane with 0.2 μm pore size. Reprinted with the permission from Png et al. (2015) ©The Optical Society, 2015

pipetted onto the thin membrane, it will spread out resulting in poor color visibility. Commercially, the nitrocellulose membrane is available in the range of 100–150 μm thickness (Mansfield 2009).

Pore size is directly related to the particle retention capabilities of the paper. Pore size can be determined experimentally using the bubble point method (Yu et al. 2010). In this method, after soaking the porous structure of the membrane into liquid, air pressure is applied to transport the fluid into the pores of the membrane. The minimum pressure at which first air bubble is formed corresponds to the largest diameter of the pore in the filtration direction of the membrane, known as bubble point. At this point, the nominal pore size can be calculated from the following equation: $d = \frac{4\gamma \cos\theta}{P}$, where d is the average pore diameter, γ is the liquid surface tension, P is the minimum air pressure required to reopen the pore and θ is the

Table 2.1 Different types of paper substrates and their characteristics

Paper types	Characteristics	Applications
Whatman Filter paper grade 1	Fibrous structure, weight: 88 g m^{-2}, particle retention: >11 μm, thickness: 180 μm, porosity: 10.5 s	Detection of glucose (Kumar et al. 2017), lactate, uric Acid (Kumar et al. 2016)
Whatman Filter paper grade 2	Fibrous structure, weight: 103 g m^{-2}, particle retention: >8 μm, thickness: 190 μm	Monitoring of contaminants in the atmosphere, soil testing
Whatman Filter paper grade 3	Highly absorbent, Fibrous structure, weight: 187 g m^{-2} particle retention: >6 μm, thickness: 390 μm, porosity: 26 s	Suitable for suction filtration, used in Büchner funnels
Whatman Filter paper grade 4	Fibrous structure, weight: 96 g m^{-2}, particle retention: >25 μm, thickness: 205 μm, porosity: 3.7 s	Detection of nitrite ion (NO_2-) (Li et al. 2010)
Nitrocellulose membrane	Granular structure, reasonably uniform pore size, particle retention: >0.02 μm	Lateral flow assay, e.g. immobilization of antibody/antigen (Yen et al. 2015), DNA, enzymes, etc.
Cellulose glossy paper	Made of cellulose fiber blended with an inorganic filler, non-degradable and relatively smoother surface	Detection of ethanol (Arena et al. 2010)
Bioactive paper	Obtained by the modification of paper matrix with biomolecules	Detection of Pathogens (Pelton 2009)

contact angle between the liquid and pore wall. In actual condition, membranes contain a range of pore sizes known as pore size distribution (PSD) of the membrane. Using the PSD, the capillary flow rate can be estimated as a function of the pore size (Yetisen et al. 2013).

Porosity, a non-dimensional quantity is an inherent characteristic of the porous paper substrate. It is a measure of the extent to which its surface allows the penetration of a gas or liquid. It represents the volume fraction of open space in the paper substrate (Singh et al. 2017). Porosity can be obtained experimentally by measuring the volume of liquid absorbed by the paper substrate (Parolo et al. 2013). In this method, a paper strip of specific dimensions is dipped into a known amount of fluid such as phosphate-buffered saline (PBS). Then, the change in volume of liquid (pore volume) is measured after the strip is taken out. Finally, porosity can be calculated empirically by calculating the ratio of pore volume and the total volume of the paper.

The permeability of a porous substrate is a physical parameter that characterizes the degree of resistance to fluid flow (Rudman and Patterson 2001). The air permeability is partially dependent on the porosity. For fiber porous materials (Fig. 2.1a), it can be estimated using the following empirical relation (Van der Westhuizen and Du Plessis 1996):

$$k = r_f^2 \frac{\pi\varphi(1-\sqrt{1-\varphi})^2}{24(1-\varphi)^{1.5}} \tag{2.1}$$

where r_f is the average fiber radius. For random fibrous media, the permeability can also be calculated using the following permeability-porosity correlation (Nabovati et al. 2009).

$$k = C_1 r_f^2 \left(\sqrt{\frac{1-\varphi_c}{1-\varphi}} - 1 \right)^{C_2} \tag{2.2}$$

where φ_c is the critical value of porosity, and C_1 and C_2 are the geometrical factors of the network. Also, for the granular isotropic porous materials such as nitrocellulose membrane (Fig. 2.1d), permeability can be predicted through the Kozeny-Carman equation (Bear 2013; Choi et al. 2016).

$$k = \frac{d^2\varphi^3}{180(1-\varphi)^2} \tag{2.3}$$

2.2 Fluid Transport

Paper microfluidics deals with the fluid flow without any requirement of external force. The capillary action is the driving force for the passive movement of fluid through the paper substrate. The interaction between the paper and contacting surface of the fluid is generally governed by two opposite forces, i.e., cohesive force and adhesive force. When fluid is brought in contact with the paper, there is an intermolecular interaction between liquid molecules at the liquid–air interface (cohesion) and also between the solid-liquid interfaces (adhesion). The adhesive force is responsible for spreading of the liquid on to the porous substrate while the cohesive force such as surface tension is responsible for the reduction in the area of the liquid-air interface. So, the fluid flow occurs only when the effect of adhesion surpasses that of cohesion. The wicking depends on various physical and geometrical properties of porous media such as paper materials, the structure of the paper, pore size, permeability, paper size and shape and also on the physical properties of the liquid. In general fluid transport can be categorized in two groups namely, wet-out process and the fully wetted flow. In the first kind of flow, the fluid front is wicking along the dry porous media and can be modelled using the classical Lucas-Washburn equation. In the second case, the fluid transport occurs along the wetted porous media and is governed by the Darcy's law.

2.2.1 Classical Lucas-Washburn Equation (Capillary Flow)

Let us consider a rectangular porous paper strip of length L, uniform width w and thickness h. r_a is the average pore radius of the paper. When a small amount of liquid is dropped onto the paper substrate, three types of interfacial layer is formed due to surface tension, i.e., solid-liquid interface, liquid-vapor interface, and vapor-solid interface. The relationships between these interfacial surface tensions in an equilibrium condition (Fig. 2.2a) may be described as $\gamma_{SL} + \gamma_{LV} \cos\theta = \gamma_{SV}$, where γ_{SL},γ_{LV} and γ_{SV} are the interfacial surface tension (energy per unit area) between solid-liquid, liquid-vapor and vapor-solid interface respectively, and θ is the angle between the tangent of the liquid-vapor interface and the surface at the point of contact, known as contact angle. The contact angle is a measure of the shape of a liquid droplet on a solid surface. Generally, there are two types of liquid droplets, i.e., 'wetting' droplet $(\theta < 90°)$ and 'nonwetting' droplet $(\theta > 90°)$ and depending on its value, the surface can be either hydrophilic (liquid can wet the surface) or hydrophobic (liquid repellent surface). The chemical composition of the solid surface and liquid are the critical parameters for the contact angle.

The capillary pressure which is equal to pressure difference at liquid-solid (paper) interface in the wetted region is governed by the Laplace pressure (Washburn 1921),

$$\mathrm{P_c} = \frac{2\gamma\cos\theta}{\mathrm{r_a}} \tag{2.4}$$

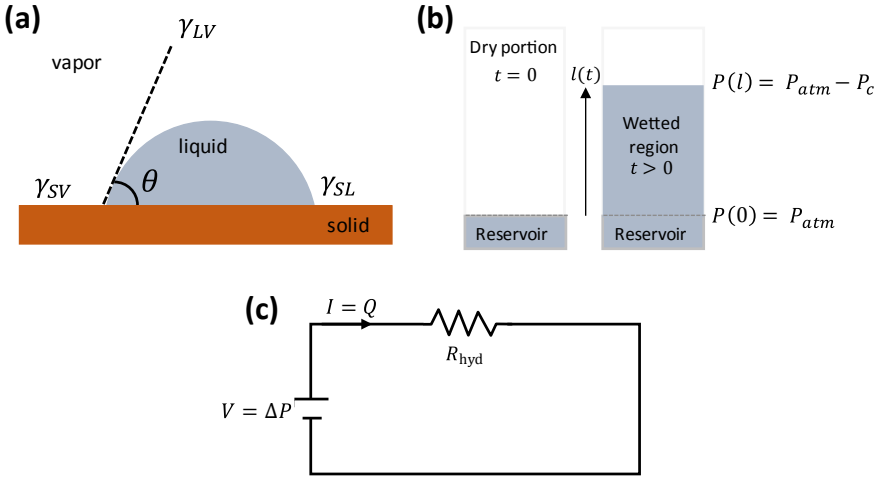

Fig. 2.2 **a** Surface tension force balance at a three-phase contact line between a liquid droplet, its vapor, and a non-deformable solid surface. **b** Schematic of fluid flow in a paper strip (porous media) through capillary action. **c** Electrical circuit analogy (Ohm's law) for fluid transport in a paper-based fluidic circuit

where γ is the interfacial surface tension of the liquid, and r_a is the average pore radius. For the dynamic systems, the contact angle may not have a static value and depends on the meniscus velocity (the Capillary Number Ca). (Fries and Quéré 2010) The dynamic contact angle can be determined by an empirical relationship proposed by Jiang et al. (1979) (based on data by Hoffman 1975),

$$\frac{\cos\theta_d - \cos\theta}{\cos\theta + 1} = -\tanh\left(4.94\mathrm{Ca}^{0.702}\right) \tag{2.5}$$

At the onset of capillary flow, the average liquid velocity is very small and assumed to be zero and therefore, the contact angle remains constant. Now, by neglecting the gravity effect and the inertial terms and combining Eq. (2.4) and the Hagen-Poiseuille's equation for fully developed flow with capillary action caused by surface tension, the penetration/wetted length of one-dimensional single phase fluid transport in paper substrate can be described by the classical Lucas-Washburn equation as (Mendez et al. 2009),

$$l(t) = 2\sqrt{\frac{k\gamma\cos\theta}{\varphi\mu r_a}}\sqrt{t} \tag{2.6}$$

where $l(t)$ is the length of wetted region of the paper after time t, k is the permeability of the paper which is a measure of how easily fluid can flow through a given paper substrate and depends upon pore size and pore geometry, μ is the fluid viscosity and t is the liquid penetration time. Equation (2.6) is derived under some assumptions such as single-phase homogenous one-dimensional fluid flow in a constant temperature and ambient pressure, perfectly wetting fluid, a uniform cross-section of the porous surface, no frictional or inertia losses due to the displacement of air by liquid, no viscosity induced pressure losses, etc. Since γ, θ, μ and r_a are all constant for a given fluid wicking through a given paper substrate, so, the wicking length is proportional to square root of time ($l(t) \propto \sqrt{t}$), i.e., the fluid-front velocity decreases with time because of the flow resistance offered by the surface of porous media (Fu et al. 2011).

The Lucas-Washburn equation is a fundamental equation for modelling the fluid flow in porous media. By considering the effect of tortuosity on the capillary flow, the Lucas-Washburn equation can be expressed in following form,

$$l(t) = \sqrt{\frac{r_a\gamma\cos\theta}{2\mu\tau^2}}\sqrt{t} \tag{2.7}$$

where tortuosity $\tau = (L_e/L)^2$, L_e effective path length between two intermittent points in the liquid and L straight path length. The value of τ is always greater than one.

2.2.2 Darcy's Law for Fluid Flow

The fluid flow through the fully wetted paper substrate is described by the Darcy's law. It was first established experimentally by Henry Darcy in 1856. By investigating the flow of water through sand, it was found that the viscous pressure loss can be described by

$$\boldsymbol{u} = -\frac{k}{\mu}\nabla P \tag{2.8}$$

where $\boldsymbol{u}$ is the average fluid velocity vector, k is the medium permeability, μ fluid viscosity, and P is the pressure. On further expanding, the above equation, the imbibition rate of the fluid ($\widehat{u}$) through the paper substrate can be determined by Darcy's law, as per the following equation,

$$\widehat{u} = \frac{k_i \Delta P}{\mu l(t)} \tag{2.9}$$

where $k_i = \frac{k}{\varphi}$ is the interstitial permeability of the paper strip, $\varphi = 1 - \frac{m}{\rho_c h}$ is the porosity of the medium(Hong and Kim 2015), m is the basis weight, ρ_c and h are the density and thickness of the porous substrate, and ΔP is the pressure difference over the wetted region known as Laplace pressure. Darcy's law describes the flow rate Q for a fluid through a porous medium (Fig. 2.2b) under a pressure differential ΔP. The relationship can be derived from the Navier–Stokes equation (Fu et al. 2011),

$$\mathrm{Q} = -\frac{kwh}{\mu L}\Delta P \Rightarrow \Delta P = -\frac{\mu L}{kwh}Q \tag{2.10}$$

In this expression, $\Delta P = P(0) - P(l)$, where $P(0)$ is the pressure at x = 0, and $P(l)$ is the average capillary pressure at the fluid front, $w \times h$ is the cross-sectional area of the paper strip. The flow domain for the considered model system also includes a hydrodynamic load term, which involves a generic flow resistance $R_{hyd} = \frac{\mu L}{kwh}$ at satisfies,

$$Q = -\frac{\Delta P}{R_{hyd}} \tag{2.11}$$

Equation (2.11) is an analogous to the Ohm's law of an electric circuit,$\Delta V = RI$, where I is the electric current, R is the electrical resistance and ΔV is the potential drop (Fig. 2.2c). In hydrodynamic systems the volumetric flow rate, Q is the volume per unit time, while in electric system current is the charge per unit time. Also, ΔP (energy per volume) is analogous to potential drop (energy per charge).

Table 2.2 List of the relevant dimensionless numbers for paper-based microfluidics

Numbers	Equations	Forces	Characteristics
Capillary number (Ca)	$\frac{\mu v}{\gamma}$	$\frac{\text{viscous}}{\text{surface tension}}$	Describes the capillary flow
Weber number (We)	$\frac{\rho v^2}{\gamma/r_a}$	$\frac{\text{dynamic pressure}}{\text{capillary pressure}}$	Predicts the disruption of an interface under the action of inertial forces
Reynolds number (Re)	$\frac{\rho v d}{\mu}$	$\frac{\text{advective mass transport}}{\text{momentum transport}}$	Describes the flow regime. Predicts whether the system will be dominated by viscosity or momentum
Schmidt number (Sc)	$\frac{\mu}{\rho D}$	$\frac{\text{momentum transport}}{\text{diffusive mass transport}}$	Describes the mass-momentum transfer
Péclet number (Pe_L)	$\text{Re} \times \text{Sc} = \frac{v}{D/d}$	$\frac{\text{advective mass transport}}{\text{diffusive mass transport}}$	Describes the diffusion and appears in mixing phenomena

The Darcy law is only valid for small Reynolds numbers where convective terms can be neglected and viscous terms dominate. Due to the varying pore geometries of the paper, no specific critical pore Reynolds number can be provided for the validity of the Darcy law, as they vary between 0.1 and 75 (Dullien 2012). Table 2.2 lists the some important dimensionless numbers related to paper-based microfluidics.

2.2.3 *Fluid Transport in the Porous Media of Varying Cross Section/Arbitrary Shape*

Apart from the straight channels, various researchers have proposed alternative models to govern the fluid transport through the paper strips with different shapes with specific dynamics such as circular (Conrath et al. 2010), trapezoidal (Mendez et al. 2009), sector-shaped (Wang et al. 2013), multi-section medium (Shou et al. 2014), and other arbitrary shapes (Elizalde et al. 2015). For n number of connected rectangular paper strips with a piecewise varying cross-section (Fig. 2.3a), the volumetric flow rate can be evaluated using the equation,

$$Q = -\frac{k\Delta P}{\mu \sum_{i=1}^{n} L_i/w_i h_i} = \frac{\Delta P}{\sum_i^n R_{hyd_i}} \tag{2.12}$$

The total time required to transport the fluid through the entire length (L) of the paper strip is given by

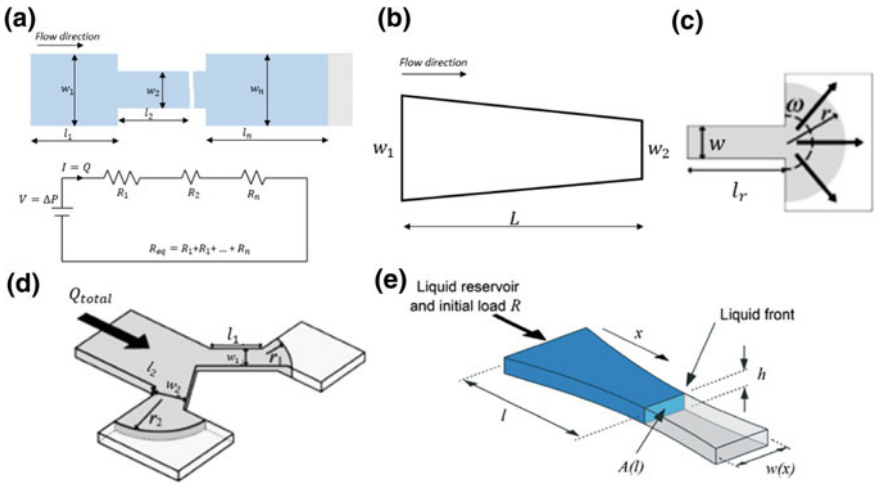

Fig. 2.3 Schematics of paper strips with various shapes. **a** Piecewise varying width, **b** Trapezoidal, **c** Fan-shape, **d** Y-shape, and **e** Paper strip with non-uniform cross-section. Reproduced from Elizalde et al. (2015) with permission from the Royal Society of Chemistry

$$t' = \frac{\mu}{k\Delta P}\left(\sum_{i=1}^{n} w_i L_i\right)\left(\sum_{j=1}^{n} \frac{L_j}{w_j}\right) \tag{2.13}$$

The fluid flow time in paper substrate of trapezoidal shape (Fig. 2.3b) can be estimated using the following equation (Shou et al. 2014),

$$t = \frac{L^2 w_1^2 C}{4(w_1 - w_2)^2}\left\{\left(\frac{w_2^2}{w_1^2}\right)\left[\ln\left(\frac{w_2^2}{w_1^2}\right) - 1\right] + 1\right\} \tag{2.14}$$

where C is a constant term equal to $\mu/\left(J(s)\gamma\cos\theta\sqrt{k/\varphi}\right)$, where $J(s)$ is a Leverett J-function of water saturation. The volumetric flow rate for a straight paper channel connected with a fan-shaped expansion zone (Fig. 2.3c) can be calculated by (Mendez et al. 2009),

$$Q = \frac{kh\Delta P}{\mu}\left[\frac{l_r}{w} + \frac{1}{\omega}\ln\left(\frac{2r}{w}\right)\right]^{-1} \tag{2.15}$$

where l_r and w are length and width of the straight portion of the paper, ω is the central angle of the fan and r is the radial distance of imbibition in the expansion zone. Equation (2.15) can be further modified by taking into account the hydrophobic outer boundaries into paper strip (Hong et al. 2016).

$$Q = \frac{khA\Delta P}{\mu}\left[\frac{l_r}{\alpha_r w} + \frac{1}{\alpha_s \omega}\ln\left(\frac{2r}{w}\right)\right]^{-1} \tag{2.16}$$

where α_r and α_s reduction coefficients corresponding to the straight channel and expansion zone, respectively. The reduction coefficient (α) is defined as the ratio of imbibition rate through a paper channel with and without the wax boundaries. The value of α_s is be assumed to be 1 for a large channel width (>3 mm). Also, since $\alpha_r < 1$, so Eq. (2.16) suggests the volumetric flow rate is reduced in a paper channel with wax boundaries. The first term within the bracket in right-hand side of Eq. (2.16) is associated with flow resistance in the straight channel (R_s) while the second term is associated with the flow resistance in expansion zone (R_e). Since the value of r in flow resistance term for expansion zone varies with wetted length and time t, so the flow rate would be unsteady this term is dominant. However, if $R_s \gg R_e$ then fluid transport through the channel can be assumed as a steady flow.

The volumetric flow rate for flow bifurcation system as shown in Fig. 2.3d can be written as $Q = Q_1 + Q_2$. It can also be described in terms of hydrodynamic flow resistance.

$$\frac{Q_2}{Q_1} = \frac{R_1}{R_2} = \frac{\frac{l_1}{\alpha_1 w_1} + \frac{1}{\omega}\ln\left(\frac{2r_1}{w_1}\right)}{\frac{l_2}{\alpha_2 w_2} + \frac{1}{\omega}\ln\left(\frac{2r_2}{w_2}\right)} \tag{2.17}$$

For a specified fluid velocity or mass transport rate the cross-sectional shape of the paper strip can also be estimated using the empirical model developed by Elizalde et al. (2015). Figure 2.3e shows the schematic of the flow domain used for modeling. The time required for imbibition of fluid in a paper strip of varying cross-section $A(x)$ and length (l) is described as:

$$\frac{kR}{\mu}\int_0^l A(l')dl' + \int_0^l \left[A(l')\int_0^{l'}\frac{dx}{A(x)}\right]dl' = Dt \tag{2.18}$$

where R is the flow resistance, and D is the diffusive coefficient, a constant term in this model which is equal to $k\Delta P/\mu$. Applying the Leibniz rule, Eq. (2.18) can be converted into following expression to obtain an explicit solution for the unknown cross-sectional profile $A(x)$ of the paper strip to attain a desired flow rate $Q(x)$:

$$A(x) = -\frac{Q(x)^2}{D}\left[\frac{dQ(x)}{dx}\right]^{-1} \tag{2.19}$$

By putting the $Q(x) = v(x)A(x)$ the equation was further expanded into:

$$A(x) = \frac{v_0 A_0}{v(x)} \exp\left[-\frac{1}{D}\int_0^x v(x')dx'\right] \tag{2.20}$$

where $v(x)$ is the velocity function, v_0 and A_0 are the velocity and cross-sectional area at x = 0 respectively. These equations can be used to determine the unknown cross-sectional shape required for a specified fluid velocity $v(x)$ and mass flow rate $Q(x)$.

2.2.4 Radial Fluid Transport in Porous Media

When a drop of liquid penetrates into the surface of the paper substrate for the first time, it wicks radially outward. Unlike, the cylindrical capillary, the liquid-vapor interfacial area continuously increases with time in radial flow. The radial penetration of liquid in thin porous media was theoretically studied for the first time by Marmur (1988). Since then, many researchers have theoretically and experimentally investigated the radial capillary transport mechanism in the porous substrate (Conrath et al. 2010; Xiao et al. 2012; Wang et al. 2013; Kumar et al. 2016). Conrath et al. (2010) developed a theoretical model to estimate the time required to reach the liquid by radial wicking in a paper strip of desired radius R (Fig. 2.4a) which is given as:

$$t(r) = \frac{r_a \mu \varphi R^2}{8\gamma k h \cos\theta}\left[\ln\left(\frac{r(t)}{r_0}\right)^2 + \left(\frac{r_0}{r(t)}\right)^2 - 1\right] \tag{2.21}$$

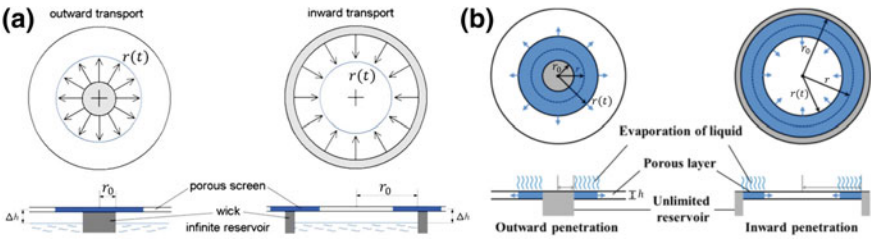

Fig. 2.4 **a** Schematic illustration for outward (left side) and inward (right side) capillary fluid transport. Reprinted from Conrath et al. (2010) with permission from ©Springer Science + Business Media B.V. 2009. **b** Radial capillary penetration incorporating evaporation. Reprinted with permission from Liu et al. (2016) ©2016 American Chemical Society

where $r(t)$ and r_0 are the radii of the wetted fluid front at time t and the liquid reservoir, respectively. This relation can be further utilized to predict the volumetric flow rate of circular wicking front in a paper substrate,

$$Q = \frac{2\pi k\gamma h\cos\theta}{\mu \ln\left(\frac{r(t)}{r_0}\right)^2} \tag{2.22}$$

If the ambient condition like, evaporation effect is taken into account, then the radius up to which the fluid penetrates radially in thin layer porous medium (Fig. 2.4b) for the given evaporation rate can be determined as (Liu et al. 2016),

$$\left(\frac{r_c}{r_0}\right)^2\left[1-2\ln\left(\frac{r_c}{r_0}\right)\right] = 1-\frac{\dot{m}_e^c}{\dot{m}_e} \tag{2.23}$$

where R_c is the critical radius, $\dot{m}_e$ and $\dot{m}_e^c$ are actual and critical evaporation rate of liquid respectively. The critical evaporation rate which depends on the liquid properties, physical and geometrical parameters of the porous medium, can be estimated using the following equation,

$$\dot{m}_e^c = \frac{4\sigma\cos\theta_s\rho}{\mu}\frac{2k}{r_{eff}}\frac{h}{r_0^2} \tag{2.24}$$

where r_{eff} is the effective pore radius of the porous medium.

2.2.5 Diffusion-Based Fluid Transport

In case of mass transport in the paper substrate, the behavior of fluids can't be fully predicted by the Navier-Stokes equation as it does not consider diffusion. The motion of a chemical or biochemical species in the wetted paper matrix are described with a set of governing equations.

Fick's first law of diffusion:

$$J_i = -D\frac{\partial C_i}{\partial x} \tag{2.25}$$

Fick's second law of diffusion:

$$\frac{\partial C_i}{\partial t} = D\nabla^2 C_i \tag{2.26}$$

Here, the quantity J_i is the flux of solute i, C_i is the concentration of solute i in mass per unit volume. The quantity D is the diffusion coefficient of the solute in the carrier fluid, which can be estimated by the Stokes-Einstein relation. $D = \frac{kT}{6\pi\eta r_h}$, where k is a Boltzmann constant, T is the temperature, η fluid viscosity, and r_h is the hydrodynamic radius of the solute. In the equation, the term in the numerator represents the kinetic energy of the molecule, while the denominator represents the friction force acting on the molecule. Fick's second law governs the change in concentration field with time due to the diffusion. For the capillary pressure driven flow, the Fick's second law can be formulated as

$$\frac{\partial C_i}{\partial t} + \boldsymbol{u}\nabla C_i = D\nabla^2 C_i \tag{2.27}$$

This is known as a convection-diffusion equation. The diffusive flow field can be modeled using the above equation with specified boundary conditions. The mass transfer in the moving fluid through the porous media are generally governed by the molecular diffusion and by the fluid velocity field. The Péclet number (Pe_L) plays a vital role in mass transport phenomena. If $Pe_L < 100$, the mass transport is controlled by the molecular diffusion and if $Pe_L \geq 100$, mass transport is controlled by the average fluid velocity (Piquemal 1993).

2.2.6 *Lateral Flow Immunoassay (LFIA)*

Lateral flow assay (LFA) based POC devices is the fastest growing technology for qualitative and quantitative analysis. According to the Markets and Markets report, the lateral flow assay had covered 28.2% of the global market for clinical diagnostics of infectious diseases in 2016. The LFIA based market is expected to reach $8.24bn by 2022 from an estimated $5.55bn in 2017, at a compound annual growth rate of 8.2%. (Lateral Flow Assay Market worth 8.24 Billion USD by 2022 August 2017) From the past several years, the lateral flow-based immunoassays have garnered much attention in diagnostics of infectious diseases such as malaria, dengue (Wang et al. 2014; Zhang et al. 2015; Kumar et al. 2018), Ebola (Yen et al. 2015), HIV, Zika (Bosch et al. 2017), etc.

Components and Principles

The LFIA biosensing platform mainly consists of four components namely, sample pad, conjugate pad, nitrocellulose membrane, and an absorbent pad, which are all held together on a plastic backing card using a pressure-sensitive adhesive with a specified overlap onto one another (Fig. 2.5a). The component overlaps allow the unrestricted capillary flow of the samples from the sample pad to the absorbent pad.

Sample pad's primarily role is to transport the target analyte to other components of LFA with high efficiency and providing the homogeneous distribution of the sample onto the conjugate pad. It also controls the fluid flow rate. It is generally

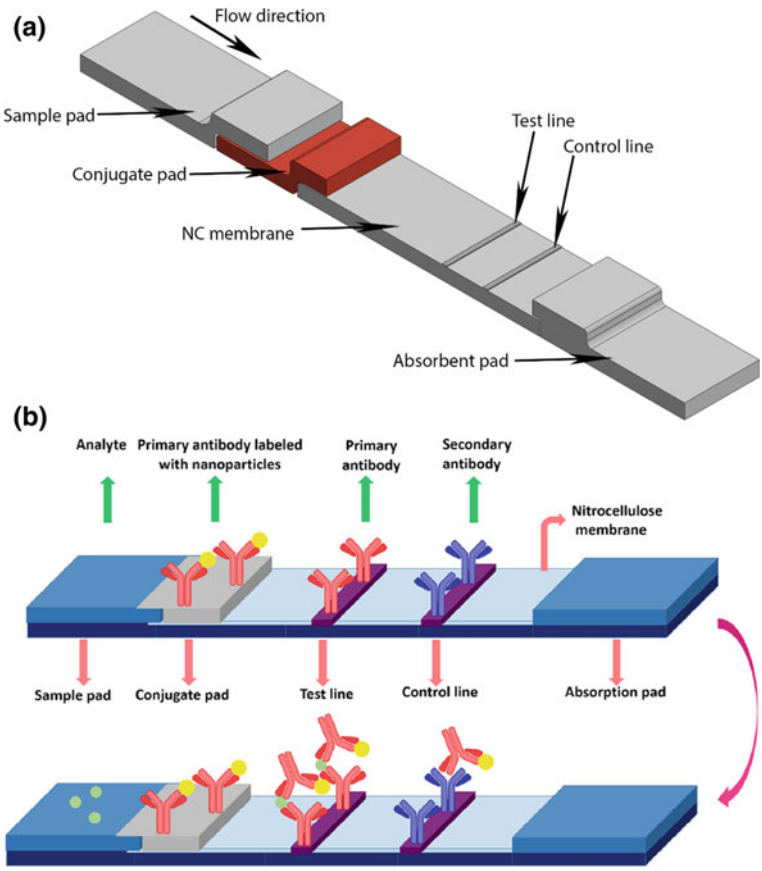

Fig. 2.5 **a** Typical configuration of the lateral flow test strip. **b** Schematic of sandwich format of LFIA. Reprinted from Bahadır and Sezgintürk (2016) with permission from Elsevier B.V.

made of cellulose, rayon, glass fiber, woven meshes, Whatman filter paper grade 1, etc. The choice of material for the sample pad depends on the sample types which is to be handled.

The role of conjugate pad is to allow the immobilization of nanoparticles-Ab conjugates, holds the conjugates for a long time in dried form and releasing the labeled conjugate efficiently upon contact with the incoming aqueous sample from sample pad. So, the hydrophilic porous materials with high flow rates such as non-woven filters, glass fiber, cellulose, rayon, polyesters, polypropylene, etc. are used in the fabrication of conjugate pad.

The membrane is an essential and critical component of the lateral flow test strip. The primary purpose of the membrane is to allowing its surface for binding of proteins at the test line and control line. Nonspecific adsorption of proteins at the test and control line may results in reduced sensitivity, so an ideal membrane should

have the high protein-binding capacity. Nitrocellulose membrane is most widely used material for the membrane fabrication. It binds protein by electrostatic interaction between strong dipole of the nitrate ester with the strong dipole of the peptide bonds of the protein. Various types of NC membranes are available in the market with specific capillary flow time.

The absorbent pad is the engine of a lateral flow test. It helps in maintaining the capillary flow rate through the nitrocellulose membrane and prevents the backflow of excess reagents by soaking. It also allows the use of larger target sample volumes resulting in a higher sensitivity of the device. The materials used for the fabrication of absorbent pad is highly absorptive. Cellulose filters are mostly used for the absorbent pad.

Although the lateral flow assay is the one-step process, the proper selection of materials for each component, its processing and assembly are very crucial. The optimization of experimental conditions is needed to develop a LFA test strip with excellent performance and high sensitivity (Bahadır and Sezgintürk 2016).

In a typical LFIA, the target analyte such as human blood, plasma, serum, urine, saliva, etc. is loaded onto the sample pad after which it migrates to the conjugate pad which contains pre-immobilized (dried) nanoparticles-antibody (Ab) conjugates. When the sample liquid reaches the conjugate pad (CP), the antigens (Ag) present in the sample bind with the conjugated NP–Ab to form NP–Ab-Ag complexes. These complexes continue to flow towards the test line by capillary action through a nitrocellulose membrane. The test line contains immobilized capture antibody specific to Ag on it. If an antigen is present in the sample, then the antibodies on the test line conjugate with the complex making a sandwich like structure (NPs-Ab-Ag-Ab). A distinct color change can then be observed at the test line due to localized surface Plasmon resonance (LSPR) of aggregated nanoparticles. Whereas, if antigens are not present in the sample, no sandwich structure is formed resulting in no color change at the test line. The control line is loaded with secondary antibodies specific to the primary antibodies conjugated to the NPs. Here, the bounded/unbounded conjugated NPs–Ab binds with secondary antibodies (anti-IgG) to demonstrate a color change (in both cases when the antigen is present in the sample or not). The change in color at the control line confirms the successful completion of the colorimetric assay. The role of the absorbent pad is to soak up the extra liquid.

Immunochemical Reaction Mechanism

In a typical lateral flow assay, the liquid sample containing specific target analyte migrates through the sample pad and conjugate pad and reaches to the test line in detection pad. During this fluid transport, several mechanisms such as convection, molecular diffusion, immunoreactions between antibodies and antigens on the surface of reporter particles play a significant role. The sensitivity of the LFA is directly proportional to the signal intensity at the test line. The signal intensity depends on several parameters such as the concentration of reporter particles, primary and secondary antibodies, analyte flow rate, and reaction time for the target analyte to form a complex in capture site. To improve the performance of LFAs,

these terms must be considered in theoretical modeling. From the past decade, several research groups have attempted to model the surface binding mechanism involving the molecular diffusion, advective transport (movement of reactants by the bulk motion of the liquid), and chemical reactions (Hansen et al. 2012; Aguirre et al. 2014). Normally, following immunoreactions, takes place in a standard lateral flow assay. When the sample migrates through the conjugated pad, the specific target analyte (A) binds with the conjugate reporter nanoparticles-Ab/Ag (P) to form reporter nanoparticles-analyte complexes (PA).

$$[A] + [P] \rightleftarrows [PA] \tag{2.28}$$

These complexes move ahead towards the test line by capillary action through the detection pad (typically made of the nitrocellulose membrane). Test line contains immobilized capture Ab/Ag-specific to the analyte on it. At the test line, the free analyte (A_f) and conjugated nanoparticles-analyte complex (PA) interact with capture Ab/Ag (R) to form complexes RA ($[A_f] + [R] \rightleftarrows [RA]$) and RPA ($[PA] + [R] \rightleftarrows [RPA]$) respectively. Additionally, unbounded reporter particles (P_i) may bind to complex RA to form the complex RPA ($[P_i] + [RA] \rightleftarrows [RPA]$). The control probe (C) (i.e., secondary Ab specific to the primary Ab) is immobilized in control line. Here, the concentration of above complexes are functions of space x and time t (i.e., $[C](x,t)$) and can be described by the convection–diffusion–immunoreaction equations as follows (Qian and Bau 2003):

$$\frac{\partial [A]}{\partial t} = D_A \frac{\partial^2 [A]}{\partial x^2} - u \frac{\partial [A]}{\partial x} - (F_{PA} + F_{RA}) \tag{2.29}$$

$$\frac{\partial [PA]}{\partial t} = D_P \frac{\partial^2 [PA]}{\partial x^2} - u \frac{\partial [PA]}{\partial x} - \left(F_{PA} + F^1_{RPA}\right) \tag{2.30}$$

$$\frac{\partial [P]}{\partial t} = D_P \frac{\partial^2 [P]}{\partial x^2} - u \frac{\partial [P]}{\partial x} - \left(F_{PA} + F^2_{RPA}\right) \tag{2.31}$$

$$\frac{\partial [P]}{\partial t} = F_{PA} \text{ and } \frac{\partial [RPA]}{\partial t} = F_{RPA} \tag{2.32}$$

where D_A and D_P are the molecular diffusion coefficients of the analyte and the reporter particles, u is the average fluid velocity. F_{PA}, F_{RA} and F_{RPA} are the rate of formation of the particle-analyte complex and capture Ab-analyte complex respectively. F^1_{RPA} and F^2_{RPA} are the rate of formation of capture Ab-analyte-detection Ab complex due to the interactions between ($[PA] + [R] \leftrightarrow [RPA]$) and ($[P] + [RA] \leftrightarrow [RPA]$) respectively. The diffusion coefficient (D) for proteins and nanoparticles can be estimated by the Stokes-Einstein equation (Filipe et al. 2010),

$$D = \frac{\kappa_B T}{6\pi\mu R} \tag{2.33}$$

Here, κ_B is the Boltzmann constant, T is fluid temperature, μ is the fluid viscosity, and R is the hydraulic radius of the analyte or signal particle. The color signal intensity in the test line is proportional to the concentrations of reporter nanoparticles-Ab/Ag $[P]$, conjugates $[PA]$, and sandwich complex $[RPA]$ which is given as (Liu et al. 2017),

$$S = [P] + [PA] + [RPA] \tag{2.34}$$

For a given concentration of analyte, the color intensity in the test line depends on the amount of reporter nanoparticles-analyte complex reaches at the test line (Kumar et al. 2018). The optimum concentration of complex (PA) can be estimated using the following expression (Ragavendar and Anmol 2012),

$$S[PA]_{opt} = 0.9\left\{A_0 + P_0 + k_{d1}/k_{a1} - \left((A_0 + P_0 + k_{d1}/k_{a1})^2 - 4A_0P_0\right)^{0.5}\right\} \tag{2.35}$$

where A_0 and P_0 are the initial concentration of analyte in sample and concentration of conjugated Ab. k_{a1} and k_{d1} are the equilibrium reaction constants. These constants can be estimated by following expressions (Berg and Purcell 1977; Zwanzig and Szabo 1991),

$$k_{a1,particle} = \frac{4\pi aDNk_a}{Nk_a + 4\pi aD} \tag{2.36}$$

$$k_{d1,particle} = k_d\left(1 - \frac{Nk_a}{4\pi aD + Nk_a}\right) \tag{2.37}$$

where a is the nanoparticle radius, N is the number of receptors on the surface of the nanoparticle, D is the diffusion coefficient for the ligand. k_a and k_d are the association rate for complex formation and the dissociation rate constant, respectively. The convection–diffusion–immunoreaction Eqs. (2.29–2.32) and (2.35) as mentioned above, can be used in the prediction of optimized test line location where the signal intensity is maximum. Several recent publications reported the numerical models for lateral flow assay. Berli and Kler (2016) developed a quantitate LFA model for predicting the relative concentration of antigen-antibody complex at the test line. Liu et al. (2017) developed a one-dimensional mathematical model to study the effect of report particle characteristics like the binding sites on the overall performance of LFAs. They successfully validated their model with the experimental results. Schaumburg et al. (2018) reported a three-dimensional multi-membrane model for lateral flow assays. Liu et al. (2018) developed a

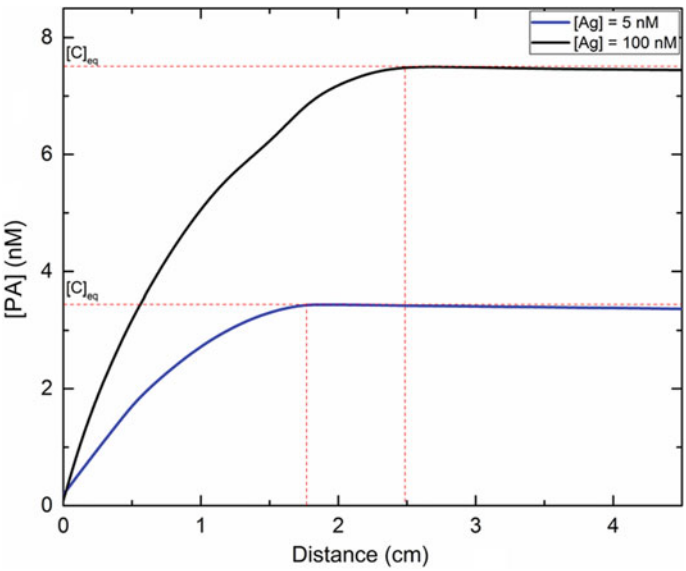

Fig. 2.6 Variation of the concentration of conjugated complex as a function of fluid transport distance along the nitrocellulose membrane for capillary flow time = 200 s/4 cm. Reprinted with permission from Kumar et al. (2018), ©Author(s)

semi-quantitative convection-diffusion-reaction model to investigate the effect of inlet reporter particle concentration, initial capture probe concentrations and association rate constant on overall performance of the lateral flow device. The association and dissociation rate constants were calculated by considering the kinetics of renaturation of nucleic acids. They were able to theoretically estimate the detection limit of the device and validated by direct comparison with experimental data.

In recent times, researchers have utilized the convection–diffusion–immunoreaction models to design the lateral flow assay for point-of-care diagnostic applications. Kumar et al. (2018) utilized the convection–diffusion–immunoreaction model to optimize the dimensions of the lateral flow device. The location of the test line was theoretically estimated and successfully validated by experimentation. The test line distance was optimized such that sufficient reaction time is given to the conjugated complex (PA) to achieve equilibrium concentration since, after that, no change in [PA] occurs (Fig. 2.6). Based on the theoretical study, they presented a unique lateral flow immunoassay device that used a tapered NC membrane and gold nanoparticles-graphene oxide (Au-rGO) nanocomposite as a detection label for highly sensitive detection of dengue NS1.

2.3 Summary

Paper-based microfluidic systems are one of the most widely used technology in the field of point-of-care diagnostics. The transport of fluid containing molecules, particles, analytes, etc. is a critical process in several paper-based microfluidic devices. The theoretical understanding of fluid transport phenomena helps in designing of a paper-based device. The capillary-based wicking phenomena of paper substrates theoretically eliminate the requirement of external equipment for fluid transport. This chapter provides a theoretical background of fluid transport in paper substrates, paper types, critical parameters involved in fluid flow, etc. This chapters also gives a brief overview of different kinds of governing equations used in designing of paper-based devices.

The present brief overview may aid in providing physically and synthetically intuitive guidance for the design of paper-based microfluidic devices such as dip-stick assays, lateral flow assays, etc. with a high sensitivity and wide working range.

References

Aguirre A, Kler PA, Berli CL, Collins SE (2014) Design and operational limits of an ATR-FTIR spectroscopic microreactor for investigating reactions at liquid–solid interface. Chem Eng J 243:197–206

Altundemir S, Uguz A, Ulgen K (2017) A review on wax printed microfluidic paper-based devices for international health. Biomicrofluidics 11(4):041501

Arena A, Donato N, Saitta G, Bonavita A, Rizzo G, Neri G (2010) Flexible ethanol sensors on glossy paper substrates operating at room temperature. Sens Actuator B-Chem 145(1):488–494

Bahadır EB, Sezgintürk MK (2016) Lateral flow assays: principles, designs and labels. Trends Anal Chem; TrAC, 82:286–306

Bear J (2013) Dynamics of fluids in porous media. Courier Corporation

Berg HC, Purcell EM (1977) Physics of chemoreception. Biophys J 20(2):193–219

Berli CL, Kler PA (2016) A quantitative model for lateral flow assays. Microfluid Nanofluidics 20 (7):1–9

Bosch I, de Puig H, Hiley M, Carré-Camps M, Perdomo-Celis F, Narváez CF, Salgado DM, Senthoor D, O'grady M, Phillips E (2017) Rapid antigen tests for dengue virus serotypes and Zika virus in patient serum. Sci Transl Med 9(409):eaan1589

Choi JR, Liu Z, Hu J, Tang R, Gong Y, Feng S, Ren H, Wen T, Yang H, Qu Z (2016) Polydimethylsiloxane-paper hybrid lateral flow assay for highly sensitive point-of-care nucleic acid testing. Anal Chem 88(12):6254–6264

Conrath M, Fries N, Zhang M, Dreyer ME (2010) Radial capillary transport from an infinite reservoir. Transp Porous Med 84(1):109–132

Dullien FA (2012) Porous media: fluid transport and pore structure, 2nd edn. Academic Press, New York

Elizalde E, Urteaga R, Berli CL (2015) Rational design of capillary-driven flows for paper-based microfluidics. Lab Chip 15(10):2173–2180

Evans E, Gabriel EFM, Coltro WKT, Garcia CD (2014) Rational selection of substrates to improve color intensity and uniformity on microfluidic paper-based analytical devices. Analyst 139 (9):2127–2132

Fenton EM, Mascarenas MR, López GP, Sibbett SS (2008) Multiplex lateral-flow test strips fabricated by two-dimensional shaping. ACS Appl Mater Interfaces 1(1):124–129

Filipe V, Hawe A, Jiskoot W (2010) Critical evaluation of Nanoparticle Tracking Analysis (NTA) by NanoSight for the measurement of nanoparticles and protein aggregates. Pharm Res 27(5):796–810

Fries N, Quéré D (2010) Capillary transport processes in porous materials-experiment and model. Cuvillier Verlag Göttingen

Fu E, Ramsey SA, Kauffman P, Lutz B, Yager P (2011) Transport in two-dimensional paper networks. Microfluid Nanofluidics 10(1):29–35

Hansen R, Bruus H, Callisen TH, Hassager O (2012) Transient convection, diffusion, and adsorption in surface-based biosensors. Langmuir 28(19):7557–7563

Hoffman RL (1975) A study of the advancing interface. I. Interface shape in liquid—gas systems. J Colloid Interface Sci 50(2):228–241

Hong S, Kim W (2015) Dynamics of water imbibition through paper channels with wax boundaries. Microfluid Nanofluidics 19(4):845–853

Hong S, Kwak R, Kim W (2016) Paper-based flow fractionation system applicable to preconcentration and field-flow separation. Anal Chem 88(3):1682–1687

Jiang T-S, Soo-Gun O, Slattery JC (1979) Correlation for dynamic contact angle. J Colloid Interface Sci 69(1):74–77

Kumar S, Bhushan P, Bhattacharya S (2016) Development of a paper-based analytical device for colorimetric detection of uric acid using gold nanoparticles–graphene oxide (AuNPs–GO) conjugates. Anal Methods 8(38):6965–6973. https://doi.org/10.1039/c6ay01926a

Kumar S, Bhushan P, Bhattacharya S (2017) Facile synthesis of Au@Ag-Hemin decorated reduced graphene oxide sheets: a novel peroxidase mimetic for ultrasensitive colorimetric detection of hydrogen peroxide and glucose. RSC Adv 7:37568–37577. https://doi.org/10.1039/c7ra06973a

Kumar S, Bhushan P, Krishna V, Bhattacharya S (2018) Tapered lateral flow immunoassay based point-of-care diagnostic device for ultrasensitive colorimetric detection of dengue NS1. Biomicrofluidics 12(3):034104. https://doi.org/10.1063/1.5035113

Lateral Flow Assay Market worth 8.24 Billion USD by 2022 (August 2017) Markets and Markets. https://www.marketsandmarkets.com/PressReleases/lateral-flow-assay.asp

Li X, Tian J, Garnier G, Shen W (2010) Fabrication of paper-based microfluidic sensors by printing. Colloids Surf, B 76(2):564–570

Liana DD, Raguse B, Gooding JJ, Chow E (2012) Recent advances in paper-based sensors. Sensors 12(9):11505–11526

Liu Z, Hu J, Zhao Y, Qu Z, Xu F (2015) Experimental and numerical studies on liquid wicking into filter papers for paper-based diagnostics. AppThermEng 88:280–287

Liu M, Wu J, Gan Y, Hanaor DA, Chen C (2016) Evaporation limited radial capillary penetration in porous media. Langmuir 32(38):9899–9904

Liu Z, Hu J, Li A, Feng S, Qu Z, Xu F (2017) The effect of report particle properties on lateral flow assays: a mathematical model. Sens Actuator B-Chem 248:699–707

Liu Z, Qu Z, Tang R, He X, Yang H, Bai D, Xu F (2018) An improved detection limit and working range of lateral flow assays based on a mathematical model. Analyst 143(12): 2775–2783

Mansfield MA (2005) The use of nitrocellulose membranes in lateral-flow assays. In: Drugs of Abuse. pp 71–85

Mansfield MA (2009) Nitrocellulose membranes for lateral flow immunoassays: a technical treatise. In: Raphael CW, Harley YT (eds) Lateral flow immunoassay. Springer, pp 95–114. https://doi.org/10.1007/978-1-59745-240-3_6

Marmur A (1988) The radial capillary. J Colloid Interface Sci 124(1):301–308

Martinez AW, Phillips ST, Whitesides GM, Carrilho E (2009) Diagnostics for the developing world: microfluidic paper-based analytical devices. Anal Chem 82(1):3–10

Mendez S, Fenton EM, Gallegos GR, Petsev DN, Sibbett SS, Stone HA, Zhang Y, López GP (2009) Imbibition in porous membranes of complex shape: quasi-stationary flow in thin rectangular segments. Langmuir 26(2):1380–1385

Nabovati A, Llewellin EW, Sousa AC (2009) A general model for the permeability of fibrous porous media based on fluid flow simulations using the lattice Boltzmann method. Compos Part A Appl Sci Manuf 40(6):860–869

O'sullivan AC (1997) Cellulose: the structure slowly unravels. Cellulose 4(3):173–207

Parolo C, Medina-Sánchez M, de la Escosura-Muñiz A, Merkoçi A (2013) Simple paper architecture modifications lead to enhanced sensitivity in nanoparticle based lateral flow immunoassays. Lab Chip 13(3):386–390

Pelton R (2009) Bioactive paper provides a low-cost platform for diagnostics. Trends Anal Chem; TrAC 28(8):925–942

Piquemal J (1993) On the modelling conditions of mass transfer in porous media presenting capacitance effects by a dispersion-convection equation for the mobile fluid and a diffusion equation for the stagnant fluid. Transp Porous Med 10(3):271–283

Png GM, Fischer BM, Appadoo D, Plathe R, Abbott D (2015) Double-layered nitrocellulose membrane sample holding technique for THz and FIR spectroscopic measurements. OptExpress 23(4):4997–5013

Qian S, Bau HH (2003) A mathematical model of lateral flow bioreactions applied to sandwich assays. Anal Biochem 322(1):89–98

Ragavendar M, Anmol CM (2012) A mathematical model to predict the optimal test line location and sample volume for lateral flow immunoassays. In: 2012 annual international conference of the IEEE engineering in medicine and biology society (EMBC). IEEE, New York, pp 2408–2411

Rudman IK, Patterson TF (2001) Water and air permeability of wet sheets. IPST Technical Paper Series Number 892

Schaumburg F, Kler PA, Berli CL (2018) Numerical prototyping of lateral flow biosensors. Sens Actuator B-Chem 259:1099–1107

Shou D, Ye L, Fan J, Fu K, Mei M, Wang H, Chen Q (2014) Geometry-induced asymmetric capillary flow. Langmuir 30(19):5448–5454

Singh VK, Ravi SK, Sun W, Tan SC (2017) Transparent nanofibrous mesh self-assembled from molecular LEGOs for high efficiency air filtration with new functionalities. Small 13(6)

Van der Westhuizen J, Du Plessis JP (1996) An attempt to quantify fibre bed permeability utilizing the phase average Navier-Stokes equation. Compos Part A Appl Sci Manuf 27(4):263–269

Wang X, Hagen JA, Papautsky I (2013) Paper pump for passive and programmable transport. Biomicrofluidics 7(1):014107

Wang HK, Tsai CH, Chen KH, Tang CT, Leou JS, Li PC, Tang YL, Hsieh HJ, Wu HC, Cheng CM (2014) Cellulose-based diagnostic devices for diagnosing serotype-2 dengue fever in human serum. Adv Healthc Mater 3(2):187–196

Washburn EW (1921) The dynamics of capillary flow. Phys Rev 17(3):273–283

Xiao J, Stone HA, Attinger D (2012) Source-like solution for radial imbibition into a homogeneous semi-infinite porous medium. Langmuir 28(9):4208–4212

Yen C-W, de Puig H, Tam JO, Gómez-Márquez J, Bosch I, Hamad-Schifferli K, Gehrke L (2015) Multicolored silver nanoparticles for multiplexed disease diagnostics: distinguishing dengue, yellow fever, and Ebola viruses. Lab Chip 15(7):1638–1641

Yetisen AK, Akram MS, Lowe CR (2013) Paper-based microfluidic point-of-care diagnostic devices. Lab Chip 13(12):2210–2251

Yu J, Hu X, Huang Y (2010) A modification of the bubble-point method to determine the pore-mouth size distribution of porous materials. Sep Purif Technol 70(3):314–319

Zhang Y, Bai J, Ying JY (2015) A stacking flow immunoassay for the detection of dengue-specific immunoglobulins in salivary fluid. Lab Chip 15(6):1465–1471

Zwanzig R, Szabo A (1991) Time dependent rate of diffusion-influenced ligand binding to receptors on cell surfaces. Biophys J 60(3):671–678